

Efficient Continuous-Time Ego-Motion Estimation for Asynchronous Event-based Data Associations

Zhixiang Wang, Xudong Li, Tianle Liu, Yizhai Zhang, *Member, IEEE*,
and Panfeng Huang, *Senior Member, IEEE*

Abstract—Event cameras are bio-inspired vision sensors that asynchronously measure per-pixel brightness changes. The high temporal resolution and asynchronicity of event cameras offer great potential for estimating the robot motion state. Recent works have adopted the continuous-time ego-motion estimation methods to exploit the inherent nature of event cameras. However, most of the adopted methods have poor real-time performance. To alleviate it, a lightweight Gaussian Process (GP)-based estimation framework is proposed to efficiently estimate motion trajectory from asynchronous event-driven data associations. Concretely, an asynchronous front-end pipeline is designed to adapt event-driven feature trackers and generate feature trajectories from event streams; a parallel dynamic sliding-window back-end is presented within the framework of sparse GP regression on $SE(3)$. Notably, a specially designed state marginalization strategy is employed to ensure the consistency and sparsity of this GP regression. Experiments conducted on synthetic and real-world datasets demonstrate that the proposed method achieves competitive precision and superior robustness compared to the state-of-the-art. Furthermore, the evaluations on three 60 s trajectories show that the proposal outperforms the ISAM2-based method in terms of computational efficiency by 2.64, 4.22 and 11.70 times, respectively.

Index Terms—Event camera, continuous-time state estimation, Gaussian process regression, visual odometry.

I. INTRODUCTION

THE ego-motion estimation plays a critical role in the automated robots.

Typically, the frame-based camera is adopted to infer the ego-motion from intensity images, which is called Visual Odometry (VO) [1] or Simultaneous Localization and Mapping (SLAM) [2], [3]. Over the past decades, an implicit paradigm has formed where a visual front end tracks the sparse visual features to establish data associations, and a parallel back end triangulates landmarks from the related features and solves the Maximum A Posteriori (MAP) problem to infer the ego-motion [1]. However, the traditional frame-based feature tracking and discrete-time MAP estimation methods have a limited temporal resolution for the fixed sampling frequency. Moreover, the frame-based camera captures the instantaneous intensity of the current field view at a fixed frequency, and thus the motion information within two neighboring sampling times is almost abandoned. Although the camera with a high frame

rate can attenuate the drawback, the resulting computational consumption would be quickly intractable. Therefore, the traditional ego-motion estimation methods naturally have a limited temporal resolution.

In recent years, event cameras have emerged as a revolutionary technology in the robotics field. Unlike frame-based cameras, event cameras have an asynchronous trigger mechanism that can independently sense the illumination intensity variation at the one-pixel level. This special design brings unique benefits to the event camera, such as high temporal resolution, high dynamic range, low power consumption, resistance to motion blur, etc [4]. Nonetheless, it is challenging to realize high temporal resolution state estimation using the traditional frame-based feature tracking and discrete-time MAP estimation methods due to the aforementioned reasons. Therefore, new feature tracking and state estimation methods that exert the high temporal resolution of event cameras are imperative for event-based ego-motion estimation [5].

Asynchronous event-driven feature tracking methods [6]–[8] and Continuous-Time (CT) estimation formulas [9]–[11] have been a focus of event-based ego-motion estimation research recently. The event-based tracker independently tracks each feature in a event-by-event manner, which is triggered by asynchronous event streams rather than frame-based sampling. Meanwhile, the CT estimation formulas can naturally model the asynchronous measurements. Consequently, the temporal resolution of event cameras is retained as much as possible. Among existing CT works, two prominent methods have gathered considerable attention, i.e., the B-spline-based methods [11] and the Gaussian Process (GP)-based methods [12]. The former leverages the basic functions to interpolate the motion trajectory for the corresponding asynchronous measurements and updates the new state by adjusting the control points. In contrast, the GP-based methods adopt a Gaussian process assumption on partial system states and propagate the probabilistic states with the system state equation. Therefore, they are more flexible and have a clearer physical meaning [13]. However, the computational complexity of existing GP-based methods for event cameras is substantial, which hinders their practical deployment on robotics [10], [12].

Our proposal introduces a sliding-window optimizer for GP regression on $SE(3)$ to bound the computational complexity of event-based ego-motion estimator. A dynamic marginalization strategy is presented to maintain the sparsity and consistency of the underlying MAP problem. On this basis, an efficient CT ego-motion estimation system for asynchronous

The authors are with the Research Center of Intelligent Robotics, School of Astronautics, Northwestern Polytechnical University, Xi'an 710072, China, and also with the National Key Laboratory of Aerospace Flight Dynamics, Xi'an 710072, China (*Corresponding author: Yizhai Zhang; e-mail: zhangyizhai@nwpu.edu.cn.*)

event-based data associations is implemented to benefit the research community of event cameras and robotics. Our experimental evaluations on diverse datasets confirm that the proposed approach provides enhanced time efficiency and robustness while maintaining competitive accuracy. The key contributions of this article are summarized as follows:

- 1) A sliding-window optimizer for GP regression on $SE(3)$, which can naturally model the asynchronous measurements and have a bounded computational complexity.
- 2) A dynamic marginalization strategy for event-based CT estimation methods based on the underlying factor graph, where the sparsity and consistency is maintained.
- 3) The implementation of an efficient CT ego-motion estimation system that can estimate ego-motion from asynchronous event-based data associations. The results are sufficiently compared with the state-of-the-art.

II. RELATED WORK

Researchers have proposed different schemes to realize ego-motion estimation for event cameras, mainly including frame-like, learning-based, and continuous-time methods. Frame-like methods accumulate event streams to create some composite data structures, such as Time Surface (TS) and event frame [14]. Sparse features are then detected and tracked with a frame-like style using enhanced conventional feature-based methods [15]–[17]. Subsequently, the discrete-time back-end optimization or filtering techniques are applied to estimate the motion states. Some studies presented approaches to enhance feature tracking by directly combining the inertial measurements [18] or other sensors [19]. In addition, event-based stereo visual odometry is also studied to restore the actual scale [20], [21]. However, frame-like methods primarily treat the event-based estimation problem as a synchronous discrete-time paradigm, which limited their ability to harness the asynchronicity and high temporal resolution of event cameras.

Learning-based methods, including Convolutional Neural Network (CNN) and Spiking Neural Network (SNN), have been designed to predict optical flow from event streams [22]–[24]. A motion estimation module is attached behind the optical flow prediction module to infer the motion states. The CNN usually processes event streams in a synchronous batched manner. Consequently, the asynchronicity of event cameras largely neglected. In contrast, the SNN has an effective mechanism for encoding temporal associations from asynchronous event streams. Some unsupervised learning methods have been suggested to predict both optical flow and ego-motion [23], [24]. Typically, these SNN models require specialized neuromorphic chips for deployment and have inherent difficulty in model training. Moreover, the generalization performance of learning-based methods needs to be improved in future research [22].

CT estimation methods [25]–[28] were designed to infer the motion trajectory from asynchronous measurements and unsynchronized sensors, such as those taken from a moving car equipped with a scanning radar or multi-sensor extrinsic calibration. Recently, CT estimation methods have also been applied to event-based trajectory estimation tasks, as the event

camera itself is inherently an asynchronous sensor. Mueggler *et al.* [9] employed the B-spline to represent the CT trajectory. The estimated motion trajectory is deformed by optimizing the sparse control points to minimize reprojection errors. Subsequently, they fused the inertial measurements to further improve the accuracy and recover the scale [11].

Another important type of CT method is based on the GP regression [10], [12]. The approach has been widely applied in machine learning; therefore, the GP-based estimation methods have a potential to reveal the relations between state estimation and machine learning. Recently, Liu *et al.* [12] successfully migrated the GP-based method to event-based odometry and realized an incremental $SE(3)$ trajectory estimation scheme based on the ISAM2 optimizer. Wang *et al.* [10] proposed a sliding-window-based GP regression system combined with an outlier rejection scheme for stereo event cameras. However, the marginalization strategy is not specified designed under the sparsity consideration. As the landmarks in monocular odometry can't be simply triangulated with associated features of stereo event cameras, the temporal dependence of estimated states should be more than stereo configuration, which results in a more complex factor graph and denser Hessian matrix. Accordingly, the marginalization strategy for monocular odometry is more challenging than stereo configuration. In this paper, We introduce marginalization to ensure consistency and sparsity in probability when bounding the computational complexity.

III. METHODOLOGY

The whole system framework is overviewed in Sec. III-A. For system description, the CT trajectory estimation problem is formulated as the Maximum A Posterior (MAP) inference using asynchronous measurements as will be presented in Sec. III-B. Then, a brief explanation of the sparse GP priors factor and GP interpolated projection factor are provided in Sec. III-C and Sec. III-D, respectively. To limit the complexity of the optimization problem, Sec. III-E introduces a special designed marginal strategy.

A. System Description

The overall system pipeline primarily consists of two parallel components, i.e., 1) **Asynchronous Feature trajectory Tracking (AFT)**, and 2) **Dynamic Sliding-window Backend (DSB)** for the CT $SE(3)$ motion trajectory estimation. In the second part, those landmarks, associated with their corresponding feature trajectories, are also estimated. They are deployed as intermediate results to ultimately estimate the motion trajectory.

In the first component, event streams are fed into the AFT when the event camera is moving in the given scenario. The AFT sequentially processes these event streams in an event-by-event manner. Specifically, when an event occurs and its pixel position falls within a given corner feature's neighbor patch, the event is tracked by a single tracker that is initialized with the corner feature. Subsequently, the aforementioned template patch would move to the location of the newest tracked feature. The position of features, triggered by the same

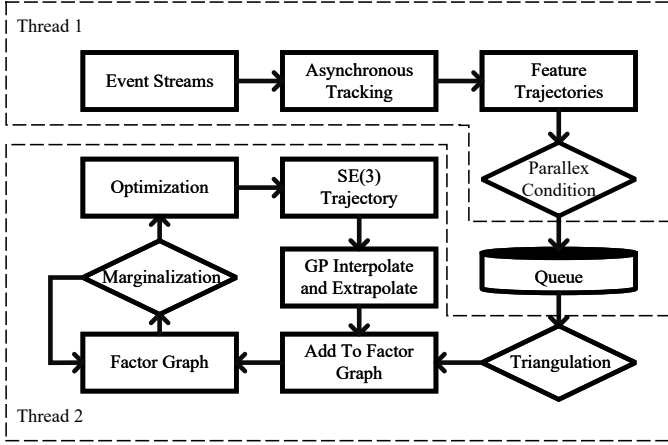


Fig. 1. System pipeline. The first thread inputs event measurements, tracks with asynchronous tracking method, and outputs feature trajectories to a queue. The second thread pops feature trajectories, tries triangulating them, and adds them into the back-end graph.

corner along with their respective timestamps, are uniquely recorded by assigning a global unique key value. The recorded positions and timestamps form a feature trajectory (as defined in Sec. III-B). Eventually, feature trajectories that meet the parallax threshold and period criteria are sent to the parallel back-end, i.e., the DSB.

In the second component, there exists several motion states in the dynamic sliding-window. To ensure the robustness of the estimation problem, a minimum size N_{min} of the sliding-window is specified. When a new motion state needs to be added to the tail of the sliding-window in the timestamp t_{k+1} , a GP extrapolation operation is carried out assuming the constant body velocity $\varpi(t_{k+1})$ (as introduced in Sec. III-C). Then, the DSB attempts to triangulate all feature trajectories within the sliding-window that have not been triangulated before. Each feature trajectory that is successfully triangulated will be assigned a 3D landmark position and joined in the back-end optimization. Specifically, each feature within the feature trajectory is incorporated into the factor graph as a GP projection factor (as explained in Sec. III-D). Moreover, a GP prior factor is established between the last motion state and the new added motion state. After constructing and optimizing the factor graph, a dynamic marginalization is executed as proposed in Sec. III-E to limit the size of the optimization problem. Finally, all state variables, involved in the factor graph, are updated with the optimized results.

B. Problem Description

When an event camera moves within a 3D scenario, a mass of asynchronous event streams will be generated. To leverage the asynchronous nature, the *feature trajectory* is recommended to describe a set of ordered features that are directly triggered by the same landmark, extracted and tracked from raw event streams (as illustrated in Fig. 2). The feature trajectory is adopted to estimate camera's CT trajectory and determine the corresponding landmark position within the

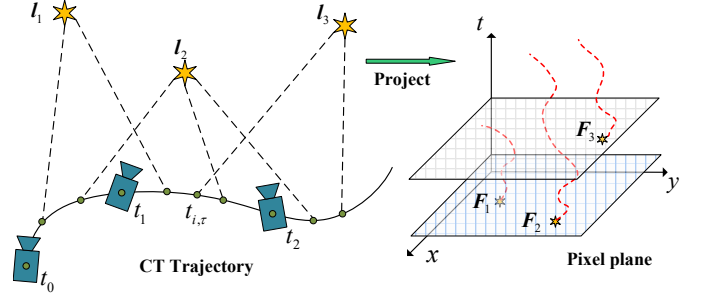


Fig. 2. An illustration of feature trajectory. When event camera moves in the space, the motion related features will generate an asynchronous measurement stream in the pixel plane which is captured at random time and disappear when feature out of visual field.

current scenario. Specifically, a feature trajectory is defined as follows:

$$\mathbf{F}_i \triangleq \langle \mathbf{m}_1^i, \mathbf{m}_2^i, \dots, \mathbf{m}_n^i \rangle, \quad (1)$$

representing an ordered spatial-temporal association set. The \mathbf{m}_τ^i indicates the τ -th tracked feature of the landmark l_i , and it contains the measurement time $t_{i,\tau}$ and pixel position $\mathbf{q}_{i,\tau} = [x_{i,\tau}, y_{i,\tau}]^\top$, i.e.,

$$\mathbf{m}_\tau^i \triangleq \{t_{i,\tau}, \mathbf{q}_{i,\tau}\}. \quad (2)$$

With the introduction of feature trajectories, our visual features exhibit arbitrary time intervals, implying that a feature trajectory may be tracked and lost at any time. As a result, the traditional processing pipeline in the frame-based visual odometry cannot be applied directly. Therefore, the GP-based CT representation is employed to deal with these asynchronous measurements for its clearly physical meaning.

Suppose a series of feature trajectories are collected from M landmarks as the camera moves according to a certain CT trajectory χ in scenario. Let \mathbf{F} be the set of these feature trajectories, where $\mathbf{F} = \{\mathbf{F}_i | i \in 0, 1, \dots, M-1\}$. The CT trajectory can be parameterized as sample points \mathbf{x}_k ($k \in \{0, 1, 2, \dots, N\}$). Given the measurement time $t_{i,\tau}$ as in (2), the corresponding motion state $\mathbf{x}(t_{i,\tau})$ can be interpolated using its neighbor states \mathbf{x}_k and \mathbf{x}_{k+1} , where $t_k \leq t_{i,\tau} < t_{k+1}$. The sum of Mahalanobis norm of GP prior residuals and the GP interpolated projection measurement residuals are minimized to obtain a maximum posterior estimation represented as

$$\min_{\chi} \left\{ \sum_{k=0}^{N-1} \|e(\mathbf{x}_k, \mathbf{x}_{k+1})\|_{\mathbf{Q}_{k+1}}^2 + \sum_{\mathbf{F}_i \in \mathbf{F}} \sum_{\mathbf{m}_\tau^i \in \mathbf{F}_i} \|e(\mathbf{x}_k, \mathbf{x}_{k+1}, \mathbf{l}_i)\|_{\mathbf{R}}^2 \right\}, \quad (3)$$

where $e(\mathbf{x}_k, \mathbf{x}_{k+1})$ indicates the GP prior residual, $e(\mathbf{x}_k, \mathbf{x}_{k+1}, \mathbf{l}_i)$ represents the visual measurement residuals, and \mathbf{Q}_{k+1} and \mathbf{R} present the covariance matrixes.

C. Sparse GP priors on SE(3)

Define the motion state as $\mathbf{x}(t) \triangleq \{\mathbf{T}(t), \varpi(t)\}$, where $\mathbf{T}(t)$ represents the matrix that transforms a vector from

the body-frame to the world-frame and $\varpi(t)$ denotes the generalized velocity in the body-frame. The White-Noise-On-Acceleration (WNOA) prior [13] is adopted to model the motion as a GP that is presented as

$$\ddot{\varpi}(t) = \mathbf{w}(t), \quad \mathbf{w}(t) \sim \mathbf{GP}(\mathbf{0}, \mathbf{Q}_c \delta(t-t')), \quad (4)$$

where $\ddot{\varpi}(t)$ is the generalized acceleration vector, \mathbf{Q}_c is a usual power spectral density matrix, and $\delta(t-t')$ is Dirac's delta function. Since $\mathbf{x}(t) \in SE(3) \times \mathbb{R}^6$ forms a manifold, it is difficult to deploy this model directly. To linearize (4), the tangent space of the estimated \mathbf{T}_k is given by

$$\mathbf{T}(t) = \mathbf{T}_k \exp(\boldsymbol{\xi}_k(t)^\wedge), \quad (5)$$

where $\exp(\bullet)$ is the exponential map from $\mathfrak{se}(3)$ to $SE(3)$ and $(\bullet)^\wedge$ maps a vector in \mathbb{R}^6 to $\mathfrak{se}(3)$ [29]. Actually, the derivative $\dot{\boldsymbol{\xi}}_k(t)$ can serve as an approximation of the body-frame velocity at a small time interval; consequently, the local linear state is defined by

$$\boldsymbol{\gamma}_k(t) \triangleq \begin{bmatrix} \boldsymbol{\xi}_k(t) \\ \dot{\boldsymbol{\xi}}_k(t) \end{bmatrix}. \quad (6)$$

Therefore, the linearized GP model can be written as

$$\dot{\boldsymbol{\gamma}}_k(t) \triangleq \begin{bmatrix} \dot{\boldsymbol{\xi}}_k(t) \\ \ddot{\boldsymbol{\xi}}_k(t) \end{bmatrix}, \quad \ddot{\boldsymbol{\xi}}_k(t) = \mathbf{w}(t) \sim \mathbf{GP}(\mathbf{0}, \mathbf{Q}_c \delta(t-t')). \quad (7)$$

When a local linear state $\boldsymbol{\gamma}_k(t)$ is given, we can use

$$\mathbf{x}(t) = \{\mathbf{T}_k \exp(\boldsymbol{\xi}_k(t)^\wedge), \mathbf{J}_r(\boldsymbol{\xi}_k(t))\dot{\boldsymbol{\xi}}_k(t)\} \quad (8)$$

to recover the true motion state, where $\mathbf{J}_r(\boldsymbol{\xi}_k(t))$ represents the right Jacobian of $\boldsymbol{\xi}_k(t)$. Under the WNOA prior, the GP prior residual within time interval (t_k, t_{k+1}) can be written as

$$e(\mathbf{x}_k, \mathbf{x}_{k+1}) = \begin{bmatrix} (t_{k+1} - t_k)\boldsymbol{\varpi}_k - \log(\mathbf{T}_k^{-1}\mathbf{T}_{k+1})^\vee \\ \boldsymbol{\varpi}_k - \mathbf{J}_r(\log(\mathbf{T}_k^{-1}\mathbf{T}_{k+1})^\vee)^{-1}\boldsymbol{\varpi}_{k+1} \end{bmatrix}, \quad (9)$$

where $\log(\bullet)$ and $(\bullet)^\vee$ are the inverse maps of $\exp(\bullet)$ and $(\bullet)^\wedge$, respectively. To maintain sparsity, a specific form of the GP prior covariance matrix is given by

$$\mathbf{Q}_{k+1} = \begin{bmatrix} \frac{1}{3}(t_{k+1} - t_k)^3 \mathbf{Q}_c & \frac{1}{2}(t_{k+1} - t_k)^2 \mathbf{Q}_c \\ \frac{1}{2}(t_{k+1} - t_k)^2 \mathbf{Q}_c & (t_{k+1} - t_k) \mathbf{Q}_c \end{bmatrix}, \quad (10)$$

which is determined in previous studies [30].

D. Visual Measurement Model

From the foregoing, we need to recover the interpolated camera state $\mathbf{x}(t_{i,\tau})$ when receiving a new measurement \mathbf{m}_τ^i . Considering the GP assumption in (7), a local linear state $\boldsymbol{\gamma}(t_{i,\tau})$ can be firstly interpolated by

$$\begin{aligned} \boldsymbol{\gamma}_k(t_{i,\tau}) &= \boldsymbol{\Lambda}(t_{i,\tau})\boldsymbol{\gamma}_k(t_k) + \boldsymbol{\Psi}(t_{i,\tau})\boldsymbol{\gamma}_k(t_{k+1}) \\ \boldsymbol{\Lambda}(t_{i,\tau}) &= \boldsymbol{\Phi}(t_{i,\tau}, t_k) - \mathbf{Q}_{i,\tau} \boldsymbol{\Phi}(t_{k+1}, t_{i,\tau})^T \mathbf{Q}_{k+1}^{-1} \boldsymbol{\Phi}(t_{k+1}, t_k) \\ \boldsymbol{\Psi}(t_{i,\tau}) &= \mathbf{Q}_{i,\tau} \boldsymbol{\Phi}(t_{k+1}, t_{i,\tau})^T \mathbf{Q}_{k+1}^{-1}, \end{aligned} \quad (11)$$

where $\boldsymbol{\Phi}(t_\tau, t_k)$ is the transition matrix [26] and $\mathbf{Q}_{i,\tau}$ is obtained through substitution of the measurement timestamp $t_{i,\tau}$ into the GP prior covariance matrix (10). Then, we can use

(8) to recover $\mathbf{x}(t_{i,\tau})$. Therefore, the predicted pixel position can be written as

$$\hat{\mathbf{q}}_{i,\tau} = \frac{1}{d_i} \mathbf{PKT}(t_{i,\tau})^\top \mathbf{l}_i + \boldsymbol{\epsilon}, \quad (12)$$

where \mathbf{K} indicates the intrinsic matrix, \mathbf{P} transforms a vector from 3D to 2D, $\mathbf{l}_i = [x_i, y_i, z_i]^\top$ is the estimated position of landmark i , d_i is the depth of the landmark in current camera frame, and $\boldsymbol{\epsilon} \sim \mathcal{N}(\mathbf{0}, \mathbf{R})$ represents the Gaussian pixel noise. Then, the measurement residual in (3) is defined by

$$e(\mathbf{x}_k, \mathbf{x}_{k+1}, \mathbf{l}_i) = \hat{\mathbf{q}}_{i,\tau} - \mathbf{q}_{i,\tau}. \quad (13)$$

E. Dynamic Sliding-Window

Existing CT estimation methods often employ an incremental smoothing (or full smoothing [11]) back-end to tackle optimization problems. However, these methods suffer from sensitivity to outliers and are computational inefficient. Inspired by discrete-time state estimation methods, we introduced an approach similar to the fixed-lag smoother [31]. More specifically, we establish a sliding-window framework and subsequently employ dynamic marginalization to eliminate redundant states upon the addition of new states. Diverging from the discrete-time paradigm, we marginalize states by considering the interconnections among feature trajectories and motion states, instead of relying on keyframes.

Algorithm 1: Dynamic Marginalization

Data: Motion trajectory $\boldsymbol{\chi}$;
 Feature trajectory set \mathbf{F} ;
 Minimum window size N_{min} ;
 Map function $\mathcal{F}(\mathbf{x}_k) \rightarrow \mathbf{F}_{k,r}$.
Result: Marginalized motion states $\boldsymbol{\chi}_m$;
 Marginalized feature trajectories \mathbf{F}_m .

```

1  $\boldsymbol{\chi}_m \leftarrow \emptyset$ ;
2  $\mathbf{F}_m \leftarrow \emptyset$ ;
3 for each  $\mathbf{F}_i$  in  $\mathbf{F}$  do
4    $\mathbf{m}_1^i = \mathbf{F}_i.front()$ ;
5    $\mathbf{m}_n^i = \mathbf{F}_i.back()$ ;
6    $t_{front} = t_{i,1}$ , where  $t_{i,1} \in \mathbf{m}_1^i$ ;
7    $t_{back} = t_{i,n}$ , where  $t_{i,n} \in \mathbf{m}_n^i$ ;
8    $t_0 = \mathbf{x}_0.timestamp$ , where  $\mathbf{x}_0 \in \boldsymbol{\chi}$ ;
9    $t_1 = \mathbf{x}_1.timestamp$ , where  $\mathbf{x}_1 \in \boldsymbol{\chi}$ ;
10   $t_N = \mathbf{x}_N.timestamp$ , where  $\mathbf{x}_N \in \boldsymbol{\chi}$ ;
11   $t_\epsilon = 0.2t_0 + 0.8t_N$ ;
12  if  $t_{back} < t_\epsilon$  and  $t_0 \leq t_{front} < t_1$  then
13     $\mathbf{F}_m \leftarrow \mathbf{F}_m \cup \{\mathbf{F}_i\}$ ;
14 for each  $\mathbf{x}_k$  in  $\boldsymbol{\chi}$  do
15   if  $N < N_{min}$  then
16     break;
17    $\mathbf{F}_{k,r} \leftarrow \mathcal{F}(\mathbf{x}_k)$ ;
18   if  $\mathbf{F}_{k,r} == \emptyset$  then
19      $\boldsymbol{\chi}_m \leftarrow \boldsymbol{\chi}_m \cup \{\mathbf{x}_k\}$ ;
20   if  $\mathbf{F}_{k,r} \neq \emptyset$  then
21     break.

```

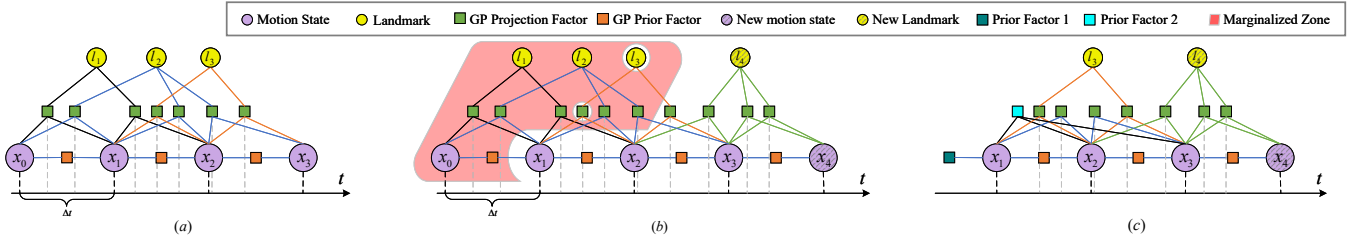


Fig. 3. Factor graph in dynamic sliding-window. (a) The original factor graph. (b) The factor graph that add new landmarks and states. The marginalized zone is marked with red shade. Notice that the node surrounded by a white ring inside the marginalized zone is not marginalized. (c) Marginalized factor graph.

The pseudocode of the marginalization algorithm is presented in Alg. 1. The function $\mathcal{F}(x_k) \rightarrow F_{k,r}$ maps a motion state x_k and its nearest neighbor x_{k+1} to their corresponding feature trajectory set $F_{k,r}$, where $F_{k,r} \subseteq F$. These feature trajectories, that are created between the initial two motion states within the sliding-window and terminate before the latest 1/5 of motion states, are considered to be marginalized (Line 3-13 in Alg. 1). Simultaneously, starting from the beginning of motion states, a motion state is marginalized if it is at the current beginning of the sliding-window and the feature trajectories directly associated with this motion state have been already marked for marginalization (Line 14-21 in Alg. 1). Furthermore, a minimum sliding-window size is maintained to prevent excessive marginalization (Line 15-16 in Alg. 1).

The special sparse structure of bundle adjustments plays a pivotal role in maintaining computational efficiency [32]. Thanks to our marginalization algorithm, we neither discard any measurements directly nor introduce new constraints between motion states and landmarks. Therefore, the structure of the resulting Hessian matrix retains its arrow-shaped form, implying that the corresponding optimization problem still have a distinct sparse structure and could be solved efficiently (as presented in Sec. IV-D). Since the resulting sliding-window size can vary with the current data-association condition, we refer to this approach as a *dynamic sliding-window* or *dynamic marginalization*.

Based on the factor graph theory, the marginalization is achieved on the linearized Markov blanket of the state variables [33]. Thus, the Markov blanket is first extracted from the original factor graph according to the state variables that should be marginalized, i.e., the outputs of the Alg. 1. Then, the linearization of Markov blanket is achieved by stacking the related hessian matrix \mathbf{H} and the vector \mathbf{b} at the current linearized point as represented in the below equation:

$$[\mathbf{H}|\mathbf{b}] = \left[\begin{array}{cc|c} \mathbf{H}_{rr} & \mathbf{H}_{rm} & \mathbf{b}_r \\ \mathbf{H}_{mr} & \mathbf{H}_{mm} & \mathbf{b}_m \end{array} \right], \quad (14)$$

where subscript r represents the reserved state variables and m denotes the marginalized counterparts. Subsequently, the Schur complement [29] can be applied to compute the marginal hessian matrix $\hat{\mathbf{H}}_{rr}$ and vector $\hat{\mathbf{b}}_r$ as follows:

$$\begin{aligned} \hat{\mathbf{H}}_{rr} &= \mathbf{H}_{rr} - \mathbf{H}_{rm}\mathbf{H}_{mm}^{-1}\mathbf{H}_{mr} \\ \hat{\mathbf{b}}_r &= \mathbf{b}_r - \mathbf{H}_{rm}\mathbf{H}_{mm}^{-1}\mathbf{b}_m. \end{aligned} \quad (15)$$

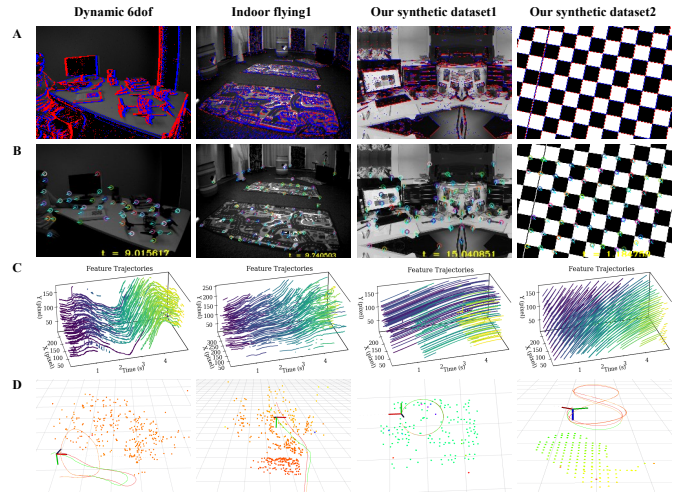


Fig. 4. Experimental scenarios and intermediate results. Scenarios and event measurements are visualized in (A). Dynamic 6dof and Indoor flying1 come from public datasets which are captured by DAVIS event cameras. The last two sequences are generated by an open-source Event camera simulator called ESIM. (B) Sparse feature points are detected and tracked by EKLt, which forms a mass of feature trajectories in 3D time-pixel-plane coordinates as shown in (C). The estimated motion trajectories and corresponding ground-truth are illustrated in (D) The pointcloud as an intermediate product is also shown in (D).

Finally, the induced marginal distribution on the Markov blanket replaces the corresponding part in the original factor graph as presented in Fig. 3.

IV. EVALUATION

A. Implementation Details

The pipeline proposed in this paper has been implemented using C++ deploying the standard non-linear optimization library *GTSAM*¹. Moreover, the GP prior factors and GP projection factors were built according to [26]. The whole system was packaged into a ROS package to facilitate the evaluation and visualization. The feature trajectory tracking was realized based on the *EKLt* [7] which use gray image in initial period and tracks each image patch with event streams asynchronously. Our evaluations are conducted on a standard computer with Intel Xeon Gold 6226R @ 3.90 GHz, Ubuntu 20.04 and ROS Noetic.

In most experiments, the time interval between neighbor trajectory points is set to $\Delta t = t_{k+1} - t_k = 0.02$ s whereas

¹<https://github.com/borglab/gtsam>

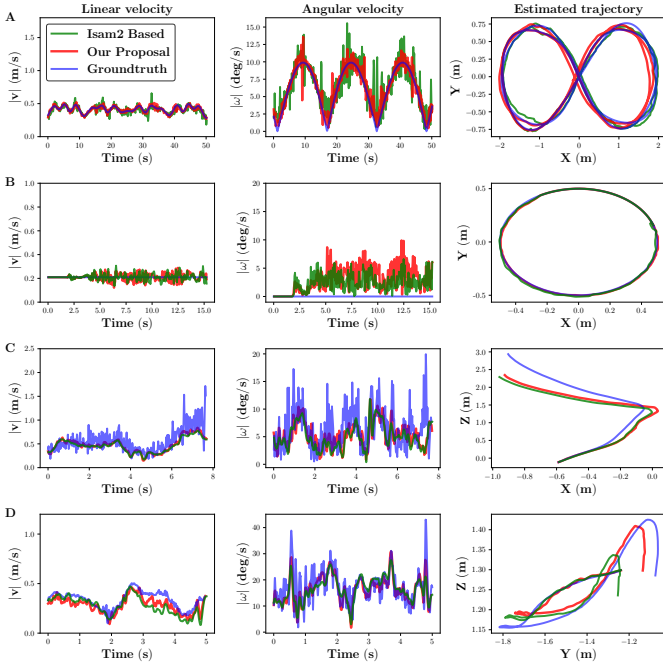


Fig. 5. Estimation results. (A) Our synthetic dataset2. (B) Our synthetic dataset1. (C) Indoor flying1. (D) Dynamic 6dof. Both linear and angular velocities are basically consistent with the ground truth. The estimated trajectories in (A) and (B) are also coincident with the ground truth, as the synthetic datasets have little noise. The noisy measurements in (C) and (D) are directly captured by a monocular DAVIS camera. As a result, the estimated trajectories are disturbed by the accumulation drift and the scale drift.

the initial number of trajectory points is set to $N = 200$. A minimum size of sliding-window is set to $N_{min} = 180$ to prevent excessive marginalization of state variables. In addition, the ground truth pose is used in initial sliding-window to initialize the whole system. Subsequently, the motion states and landmarks are estimated solely based on feature trajectories.

B. Precision and Robustness

To evaluate the precision of the proposed approach, we test it on both the synthetic datasets and the real-world event camera datasets. The synthetic datasets are generated by an open-sourced simulator, i.e., ESIM [34]. The real-world datasets include the DAVIS 240C dataset [35] and the MVSEC dataset [36] that are generated by DAVIS cameras. Moreover, the DAVIS 240C dataset consists of intensity images and ground truth from a motion capture system. As for the MVSEC dataset, it is collected using a stereo configuration with both left and right cameras (DAVIS 346B). However, the evaluation process only leverages data from the left event camera and relies on ground truth for assessment.

Experimental scenarios and feature tracking results are shown in Fig. 4A and Fig. 4B. Meanwhile, the feature trajectories described in the aforementioned section is visualized in Fig. 4C, where each color represents a different feature trajectory. The asynchronous characteristic can be illustrated from the arbitrary end time of each feature trajectory. The estimated 3D trajectories (green line) and their ground truth (red line) are

represented in Fig. 4D. The proposed monocular pipeline is confused by inherent scale drift. Nonetheless, the shape of the estimated trajectory almost coincides with its ground truth. In addition, the landmarks, estimated as intermediate products, are also displayed in Fig. 4D, which nearly coincides with their corresponding feature tracking results. In sum up, these experiments demonstrate that our proposed method has a very intuitive estimate effect.

To compare with the state-of-the-art method, the system proposed in [12] has been replicated as it is a counterpart of our asynchronous $SE(3)$ trajectory estimate method. The significant difference is that their method used an incremental back-end based on the ISAM2, and adopted *HASTE* [6] as the visual tracking method. To track feature trajectories more robustly, we replace the *HASTE* with the *EKLT*. Notice that the rest of parameters are kept consistent with our method during this comparison.

In the evaluation process, we found that the incremental method is sensitive to outliers and linear system errors. To complete the evaluation, the outliers are removed from the factor graph of the ISAM2-based method. For our monocular configuration, the Root Mean Square Relative Trajectory Errors (RMS RTE) are evaluated with a SIM(3) alignment on their estimated trajectories (as shown in Table. 1). The velocities and trajectories are visualized in Fig. 5. Generally, the precision of incremental method is competitive with our proposal. This primarily arises from the nature of the incremental approach, which ensures that no measurement information is discarded, all state variables are retained, and relinearization is allowed at any point. In contrast, our approach marginalizes partial state variables when new states are added and the preset conditions are met (as demonstrated in Alg. 1). Therefore, the estimation errors in the previous state variables could be accumulated gradually and degenerate the precision of subsequent state variables. Most importantly, the dynamic sliding-window pipeline can normally run on real-world datasets without the outlier exclusion, indicating that our method is more robust than the incremental method. The sliding-window pipeline utilizes the Levenberg-Marquardt method to solve the least squares optimization problem. To ensure the non-singularity of linear system, a scaled identity matrix has been added to the original Hessian matrix. This design feature guarantees the non-singularity of the linear system.

C. Computational Consumption

The runtime of each estimation period on previous event datasets is listed in Table. 2. Our proposal has a smaller mean and median than the ISAM2-based method in most cases. The standard deviation of our method is also smaller than the counterpart of the ISAM2-based method. It shows that our proposal gains better efficiency and has a more stable solving time than the previous method. On shapes 6dof sequence, the polygon shapes almost never move out of field view, so our marginalization condition can't be satisfied and results in a high runtime cost. Define the optimization time cost at each iteration as T_i . The total runtime of a trajectory with

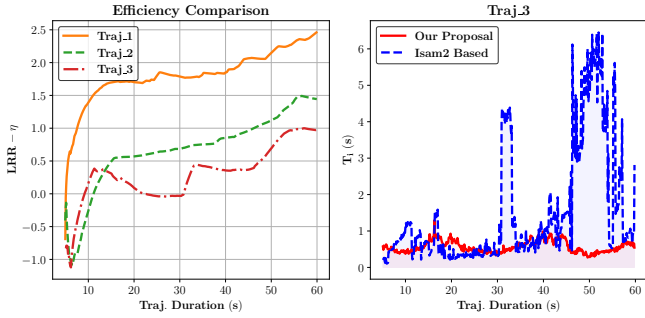


Fig. 6. Computational efficiency comparison with the ISAM2-based method.

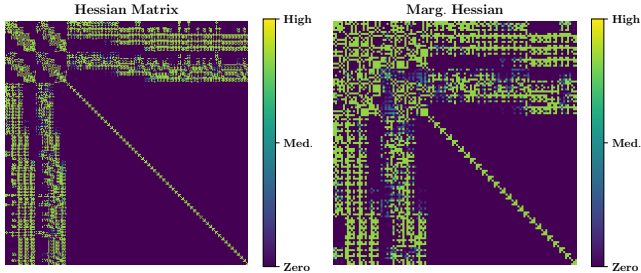


Fig. 7. Hessian matrix before and after marginalization.

N sample poses can be calculated by $\sum_{i=0}^N T_i$. Suppose the total runtime of our proposal is T_{slid} and the counterpart of ISAM2-based method (with an incremental back-end) is T_{incr} . Therefore, the Logarithmic Runtime Ratio (LRR) is given by $\eta = \ln(T_{incr}/T_{slid})$. Intuitively, $\eta > 0$ represents that our proposal is more efficient than the ISAM2-based method. The LRR are evaluated on three different 60 s trajectories. As shown in the left of Fig. 6, the LRRs at the end of trajectories are $\eta_1 = 2.46$, $\eta_2 = 1.44$ and $\eta_3 = 0.97$, respectively. It means that our method improves the computational efficiency by 11.70 (*Traj_1*), 4.22 (*Traj_2*), and 2.64 (*Traj_3*) times. Moreover, as the trajectory duration extends, the efficiency improvement will become increasingly pronounced. Another issue of the ISAM2-based method consists of the increase of computational consumption while the new state variables and measurements increase. Depending on the specific data association, the underlying Bayes tree of *ISAM2* may take lots of time to be updated. As the problem size increases, the relinearization will also become much time-consuming. Therefore, the runtime of the ISAM2-based method becomes sometimes unstable as shown in the right of Fig. 6. Inversely, the optimization problem maintains a limited scale in the proposed sliding-window-based method due to the marginalization. As the fixed-time updating is much more important for real robot’s state estimation, the proposed method has more potential to be used in future practical scenarios.

D. Sparsity Analysis

Two key factors influencing the solution efficiency of bundle adjustment are the problem’s scale and the sparsity of the corresponding Hessian matrix. To check the impact of marginalization strategy on sparsity (mentioned in Sec. III-E),

a small snap of the *Dynamic_6dof* in DAVIS 240C dataset is picked up, and the marginalization is executed where those landmarks, related with the oldest among five motion states, are marginalized as well as this oldest one. Subsequently, the corresponding Hessian matrix is visualized in Fig. 7. We see that the marginalized Hessian becomes denser while the sparse property of landmark part is still maintained; the marginalized motion state causes a reduction of 12 dimensions (6-dim for pose, 6-dim for velocity). The marginalized landmarks lead to a reduction of 102 dimensions. Considering the actual solving times depicted in Fig. 6, we draw the conclusion that the proposed marginalization strategy effectively enhances computational efficiency.

V. CONCLUSIONS

In this paper, a sliding-window pipeline based on GP regression model was proposed to estimate $SE(3)$ trajectory from asynchronous event feature tracking. The proposed method was tested and it was credible when applied to public event camera datasets and own synthetic datasets. The synthetic datasets prove that the precision of our pipeline is competitive to the incremental counterpart. More importantly, the experiments demonstrate that our proposal exhibits better robustness and computational efficiency compared to the known incremental estimate method. Although our current version can’t accomplish real-time runtime, the applied evaluation method exhibit potential capacity for future improvements. The most time-consuming process occurred while tracking features with *EKLT*. In our experiments, we found that it is unnecessary to update the tracker whenever a new event triggers. Therefore, we could solely batch the events and tracking asynchronously in each neighbor reference patch, which would be possible to realize the real-time event front-end. Since our back-end optimization problem becomes partial dense among related poses after the landmark marginalization operation, we can mitigate that by sparsifying the problem through the removal of redundant connections of state variables. Due to the Markov property of the motion state variables, the aforementioned sparsity would not compromise the original optimization problem. Furthermore, our approach can be readily extended to encompass stereo and inertial configurations in the future, which would be beneficial to inhibiting the scale drift.

REFERENCES

- [1] L. Yu, J. Qin, S. Wang, Y. Wang, and S. Wang, “A tightly coupled feature-based visual-inertial odometry with stereo cameras,” *IEEE Trans. Ind. Electron.*, vol. 70, no. 4, pp. 3944–3954, 2023.
- [2] R. Li, S. Wang, and D. Gu, “Deepslam: A robust monocular slam system with unsupervised deep learning,” *IEEE Trans. Ind. Electron.*, vol. 68, no. 4, pp. 3577–3587, 2021.
- [3] X. Zhao, Q. Li, C. Wang, H. Dou, and B. Liu, “Robust depth-aided visual-inertial-wheel odometry for mobile robots,” *IEEE Trans. Ind. Electron.*, pp. 1–11, 2023.
- [4] G. Gallego, T. Delbrück, G. Orchard, C. Bartolozzi, B. Taba, A. Censi, S. Leutenegger, A. J. Davison, J. Conrath, K. Daniilidis *et al.*, “Event-based vision: A survey,” *IEEE Trans. Pattern Anal. and Mach. Intell.*, vol. 44, no. 1, pp. 154–180, 2020.
- [5] K. Huang, S. Zhang, J. Zhang, and D. Tao, “Event-based simultaneous localization and mapping: A comprehensive survey,” *arXiv preprint arXiv:2304.09793*, 2023.

- [6] I. Alzugaray and M. Chli, "Haste: Multi-hypothesis asynchronous speeded-up tracking of events," in *Proc. Brit. Mach. Vis. Conf.*, 2020, p. 744.
- [7] D. Gehrig, H. Rebecq, G. Gallego, and D. Scaramuzza, "Asynchronous, photometric feature tracking using events and frames," in *Proc. of the Eur. Conf. Comput. Vis.*, 2018, pp. 750–765.
- [8] I. Alzugaray and M. Chli, "Asynchronous corner detection and tracking for event cameras in real time," *IEEE Robot. Autom. Lett.*, vol. 3, no. 4, pp. 3177–3184, 2018.
- [9] E. Mueggler, G. Gallego, and D. Scaramuzza, "Continuous-time trajectory estimation for event-based vision sensors," *Robot., Sci. Syst.*, 2015.
- [10] J. Wang and J. D. Gammell, "Event-based stereo visual odometry with native temporal resolution via continuous-time gaussian process regression," *IEEE Robot. Autom. Lett.*, vol. 8, no. 10, pp. 6707–6714, 2023.
- [11] E. Mueggler, G. Gallego, H. Rebecq, and D. Scaramuzza, "Continuous-time visual-inertial odometry for event cameras," *IEEE Trans. Robot.*, vol. 34, no. 6, pp. 1425–1440, 2018.
- [12] D. Liu, A. Parra, Y. Latif, B. Chen, T.-J. Chin, and I. Reid, "Asynchronous optimisation for event-based visual odometry," in *Proc. IEEE Int. Conf. Robot. Autom.*, 2022, pp. 9432–9438.
- [13] T. Y. Tang, D. J. Yoon, and T. D. Barfoot, "A white-noise-on-jerk motion prior for continuous-time trajectory estimation on $se(3)$," *IEEE Robot. Autom. Lett.*, vol. 4, no. 2, pp. 594–601, 2019.
- [14] H. Rebecq, T. Horstschäfer, G. Gallego, and D. Scaramuzza, "Evo: A geometric approach to event-based 6-dof parallel tracking and mapping in real time," *IEEE Robot. Autom. Lett.*, vol. 2, no. 2, pp. 593–600, 2016.
- [15] V. Vasco, A. Glover, and C. Bartolozzi, "Fast event-based harris corner detection exploiting the advantages of event-driven cameras," in *Proc. IEEE/RSJ Int. Conf. Intell. Robot. Syst.*, 2016, pp. 4144–4149.
- [16] W. Guan, P. Chen, Y. Xie, and P. Lu, "Pl-ivio: Robust monocular event-based visual inertial odometry with point and line features," *IEEE Trans. Autom. Sci. Eng.*, pp. 1–17, 2023.
- [17] A. R. Vidal, H. Rebecq, T. Horstschäfer, and D. Scaramuzza, "Ultimate slam? combining events, images, and imu for robust visual slam in hdr and high-speed scenarios," *IEEE Robot. Autom. Lett.*, vol. 3, no. 2, pp. 994–1001, 2018.
- [18] H. Rebecq, T. Horstschäfer, and D. Scaramuzza, "Real-time visual-inertial odometry for event cameras using keyframe-based nonlinear optimization," in *Proc. Brit. Mach. Vis. Conf.*, Sep. 2017, pp. 1–12.
- [19] P. Chen, W. Guan, and P. Lu, "Esvio: Event-based stereo visual inertial odometry," *IEEE Robot. Autom. Lett.*, vol. 8, no. 6, pp. 3661–3668, 2023.
- [20] Y. Zhou, G. Gallego, and S. Shen, "Event-based stereo visual odometry," *IEEE Trans. Robot.*, vol. 37, no. 5, pp. 1433–1450, 2021.
- [21] Y.-F. Zuo, J. Yang, J. Chen, X. Wang, Y. Wang, and L. Kneip, "Devo: Depth-event camera visual odometry in challenging conditions," in *Proc. IEEE Int. Conf. Robot. Autom.*, 2022, pp. 2179–2185.
- [22] M. Gehrig, S. B. Shrestha, D. Mouritzen, and D. Scaramuzza, "Event-based angular velocity regression with spiking networks," in *Proc. IEEE Int. Conf. Robot. Autom.*, 2020, pp. 4195–4202.
- [23] A. Z. Zhu, L. Yuan, K. Chaney, and K. Daniilidis, "Unsupervised event-based learning of optical flow, depth, and egomotion," in *Proc. IEEE/CVF Conf. Comput. Vis. Pattern Recognit.*, 2019, pp. 989–997.
- [24] F. Paredes-Vallés, K. Y. Scheper, and G. C. De Croon, "Unsupervised learning of a hierarchical spiking neural network for optical flow estimation: From events to global motion perception," *IEEE Trans. Pattern Anal. and Mach. Intell.*, vol. 42, no. 8, pp. 2051–2064, 2019.
- [25] S. Anderson, K. MacTavish, and T. D. Barfoot, "Relative continuous-time slam," *Int. J. Robot. Res.*, vol. 34, no. 12, pp. 1453–1479, 2015.
- [26] J. Dong, M. Mukadam, B. Boots, and F. Dellaert, "Sparse gaussian processes on matrix lie groups: A unified framework for optimizing continuous-time trajectories," in *Proc. IEEE Int. Conf. Robot. Autom.*, 2018, pp. 6497–6504.
- [27] Y. Wu, D. J. Yoon, K. Burnett, S. Kammel, Y. Chen, H. Vhavle, and T. D. Barfoot, "Picking up speed: Continuous-time lidar-only odometry using doppler velocity measurements," *IEEE Robot. Autom. Lett.*, vol. 8, no. 1, pp. 264–271, 2022.
- [28] D. Hug, P. Bänninger, I. Alzugaray, and M. Chli, "Continuous-time stereo-inertial odometry," *IEEE Robot. Autom. Lett.*, vol. 7, no. 3, pp. 6455–6462, 2022.
- [29] T. D. Barfoot, *State Estimation for Robotics*. Cambridge, U.K.: Cambridge Univ. Press, 2017.
- [30] S. Anderson, T. D. Barfoot, C. H. Tong, and S. Särkkä, "Batch nonlinear continuous-time trajectory estimation as exactly sparse gaussian process regression," *Auton. Robots*, vol. 39, pp. 221–238, 2015.
- [31] J. Lv, X. Lang, J. Xu, M. Wang, Y. Liu, and X. Zuo, "Continuous-time fixed-lag smoothing for lidar-inertial-camera slam," *IEEE/ASME Trans. Mechatronics*, vol. 28, no. 4, pp. 2259–2270, 2023.
- [32] F. Dellaert and M. Kaess, "Factor graphs for robot perception," *Foundations and Trends in Robot.*, vol. 6, no. 1-2, pp. 1–139, 2017.
- [33] V. Usenko, N. Demmel, D. Schubert, J. Stückler, and D. Cremers, "Visual-inertial mapping with non-linear factor recovery," *IEEE Robot. Autom. Lett.*, vol. 5, no. 2, pp. 422–429, 2019.
- [34] H. Rebecq, D. Gehrig, and D. Scaramuzza, "Esim: an open event camera simulator," in *Proc. Conf. Robot Learn.*, Oct. 2018, pp. 969–982.
- [35] E. Mueggler, H. Rebecq, G. Gallego, T. Delbruck, and D. Scaramuzza, "The event-camera dataset and simulator: Event-based data for pose estimation, visual odometry, and slam," *Int. J. Robot. Res.*, vol. 36, no. 2, pp. 142–149, 2017.
- [36] A. Z. Zhu, D. Thakur, T. Özaslan, B. Pfrommer, V. Kumar, and K. Daniilidis, "The multivehicle stereo event camera dataset: An event camera dataset for 3d perception," *IEEE Robot. Autom. Lett.*, vol. 3, no. 3, pp. 2032–2039, 2018.